ADVANCED ENGINEERING MATERIALS
www.aem-journal.com

Finite Element Modeling of Residual Stress Formation during Nanosecond Laser Ablation of Stainless Steel

Yutaka Tsumura, Anna Paradowska, Andrei V. Rode, Steve Madden, Ludovic Rapp, Meera Mohan, Alison Wain, and Gwénaëlle Proust*

Laser cleaning has recently gained attention as a non-contact, precise, and environmentally friendly method for removing contaminants, oxides, or coatings from surfaces using controlled laser ablation. However, even at low fluence, where no visible damage is observed, thermal effects from nanosecond laser pulses can induce residual stress, potentially affecting the long-term reliability of the material. This study introduces a finite element method model to predict residual stress formation in single-pulse laser ablation of stainless steel, providing detailed insight into the localized thermomechanical response. The model captures individual pulse effects, including stress evolution, thermal expansion, and localized plastic deformation. Experimental validation via X-ray diffraction is also performed. Based on this model, a parametric study is conducted to investigate the influence of pulse duration and fluence on residual stress development. The results reveal how thermal input parameters affect stress field formation and redistribution, even in the absence of visible material removal. These findings enhance understanding of stress generation in laser-processed metals and offer a framework for predicting residual stress and identifying truly damage-free thresholds in metallic substrates.

1. Introduction

Laser ablation involves the removal of material from a solid surface by irradiating it with a laser beam.[1] As a highly versatile and precise method, laser ablation is utilized across various industries for applications ranging from surface texturing[2] and micro-machining[3] to laser cleaning[4] and other material processing. The process depends on the laser parameters such as wavelength, pulse duration, and fluence, as well as the material's properties.

This article focuses on laser ablation as a method for cleaning surfaces. By carefully controlling the laser parameters, it is possible to selectively remove surface contaminants or coatings without damaging the underlying substrate.[5] The selective removal process relies on the difference in ablation threshold values between the substrate (E_s) and the surface paint/contaminant (E_c).[5] However, even when the laser fluence remains below the ablation threshold of the substrate, the thermal effects of laser pulses can still induce damage. Most studies on laser cleaning have prioritized immediately visible outcomes, such as surface cleanliness and the absence of cracks or melting. However, less attention has been paid to the less visible but equally critical issue of residual stress. These stresses are induced by the rapid heating and cooling cycles that materials undergo during laser cleaning and can have long-term implications for their structural integrity and durability.[6]

Y. Tsumura, A. Paradowska, G. Proust
School of Civil Engineering
The University of Sydney
NSW 2006, Australia
E-mail: ytsu9647@uni.sydney.edu.au

A. Paradowska
School of Aerospace
Mechanical and Mechatronic Engineering, The University of Sydney
NSW 2006, Australia

The ORCID identification number(s) for the author(s) of this article can be found under https://doi.org/10.1002/adem.202500502.

DOI: 10.1002/adem.202500502

A. Paradowska
Australian Centre for Neutron Scattering
Australian Nuclear Science and Technology Organisation (ANSTO)
Lucas Heights, NSW 2234, Australia

A. V. Rode, S. Madden, L. Rapp
Laser Physics Centre, Department of Quantum Science and Technology
Research School of Physics, Australian National University
Canberra, ACT 2601, Australia

M. Mohan
Transport for NSW
Sydney, NSW 2000, Australia

A. Wain
Centre for Creative and Cultural Research
Faculty of Art and Design, University of Canberra
ACT 2617, Australia

G. Proust
Sydney Manufacturing Hub
The University of Sydney
NSW 2006, Australia

This study examines short-pulse (SP) laser ablation, a commonly employed technique in laser cleaning that primarily operates through thermal processes. SP laser ablation often results in the formation of a heat-affected zone (HAZ) beneath the ablated surface.[7] This zone undergoes significant alterations due to the intense heat from the laser, which can lead to phase transformations,[8] microcracking,[9] and the formation of residual stresses.[10] These changes can potentially compromise the material's integrity and affect its performance in applications.

During SP laser ablation, which encompasses pulse durations from tens of picoseconds to microseconds, a series of complex mechanisms primarily govern the ablation process. These include heat conduction, radiation, melting, evaporation, and plasma formation.[11] The initiation of the ablation process is marked by the absorption of laser pulses at the material's surface, leading to a localized temperature field. This rapid temperature rise can cause the material to undergo phase transitions, transitioning into a melted, vaporized, or plasma state.[12]

This underscores the necessity for a nuanced understanding of the thermal effects induced by SP laser ablation to mitigate adverse outcomes and harness the full potential of this advanced material processing technique.

The generation of residual stress through laser processing has been the subject of numerous studies.[10] However, these investigations have predominantly relied on experimental approaches, wherein laser ablation is carried out on a target material, and the resulting residual stress is measured using techniques such as X-ray diffraction (XRD)[13] or neutron diffraction (ND).[14]

Previous studies on residual stress measurement in laser ablation of metallic materials[10b,15] have typically focused on experimental measurements across large ablation patches. These patches are generated by overlapping hundreds to tens of thousands of pulses via a raster scanning process. While informative, such approaches provide only an averaged view of residual stress generation, obscuring the fundamental mechanisms that occur at the level of a single laser pulse.

Despite the wealth of experimental data on residual stress in large-scale laser ablation, there remains a gap in our understanding of the underlying processes. This gap hinders our ability to isolate and optimize the individual mechanisms contributing to stress development, thereby limiting the precision of process control in practical applications.

The intricate dynamics of SP laser ablation, which typically occur over a few hundred nanoseconds, pose a considerable challenge not only to the tracking of residual stress generation but also to the execution of simple in-situ temperature measurements. Though there are simulation studies of nanosecond laser ablation,[16] to the best of the authors' knowledge, presently, there is no established analytical method capable of analyzing the entire sequence of phenomena occurring during the process, spanning from laser absorption, melt pool behavior, ablation profile, and formation of residual stress. This absence of a comprehensive analytical approach constitutes a significant gap in our current understanding of these processes and underscores the need for further exploration and methodological advancement in this field.

In this article, a combination of experimental analysis and numerical simulations was employed to gain a better understanding of the effect of single-spot nanosecond laser ablation. The experimental phase encompasses both laser ablation procedures and subsequent XRD measurements to assess residual stress around the ablation spots to ascertain the direct impacts of laser ablation. The finite element method (FEM) models were developed to replicate the experimental scenarios, allowing for a detailed comparison that served to validate the accuracy of the numerical models. A parametric study was then conducted to explore how variations in laser parameters influence the residual stress distribution, providing insight into optimizing laser ablation processes.

2. Experimental Section

2.1. Experimental Setup and Nanosecond Laser Ablation Parameters

The experimental investigation makes use of an austenitic stainless steel 316 (SS316) plate as the specimen. While the study was originally intended for mild steel, particularly for applications such as cleaning steel structures (e.g., buildings and bridges), SS316 was chosen to prevent oxidation and rust formation, which could compromise the reliability of the results. Given that the experiments were conducted in a series over time, stainless steel ensured consistency by minimizing surface degradation that could otherwise alter the measured residual stress distribution. This plate measures 30 mm in width, 30 mm in length, and 0.25 mm in thickness. The experiment was conducted using the Compact Phoenix Laser System from Lynton Lasers, located at the Cultural Heritage and Conservation Lab at the University of Canberra, Australia.

Figure 1 illustrates the experimental setup. This system features a Q-switched Nd: YAG laser, which is flashlamp-pumped and operates at a wavelength of $\lambda = 1064$ nm. It delivers a

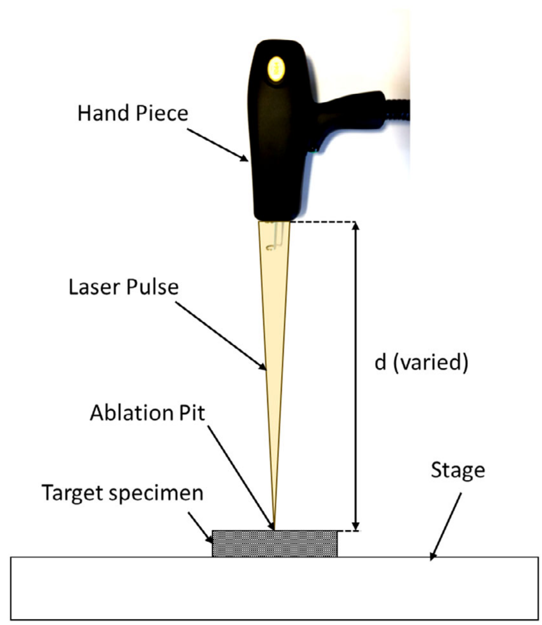

Figure 1. Schematic illustration of the laser and experimental setup.

maximum energy of $E_p = 150$ mJ ± 20% and a pulse duration of $\tau_p = 5$ ns.

The laser-generated pulses were delivered via optical fiber to a handpiece where the fiber outlet is re-imaged with a 100 mm focal lens into a fixed imaging plane at d = 120 mm away from the handpiece to a laser spot with flat-top intensity distribution and variable diameter from ≈2 mm and up to 12 mm. The pulse repetition rate f is variable from $f = 1$ Hz to $f = 10$ Hz. In addition, the laser has a burst mode where a train of three 150 mJ pulses follows each other with a time interval of 50 µs between the pulses in the train (20 kHz pulse rate within the train), generating up to 30 pulses per second. The highest fluence F over a top-hat intensity profile across the pulse diameter with the smallest laser spot on the surface is F ≈ 3.4 J cm^{-2}.

The SS316 specimen was placed directly on the stage without clamping during laser ablation to observe the material's pure thermal and mechanical response without external constraints.

2.2. XRD Residual Stress Measurements

The residual stress in the ablated specimens was investigated using the AutoMATE II micro-area stress measurement system developed by Rigaku and located at the Gunma Industrial Technology Center in Japan.

The presence of localized residual stresses on the laser-ablated surface was investigated. Stress measurements were performed at 1 mm intervals, forming a cross pattern centered on the ablation spot, including one central point and three additional points in the four cardinal directions (± x, ± y), as depicted in **Figure 2**.

The measurement of stress was done using the $\sin^2\psi$ method.[17] The $\sin^2\psi$ method is one of the most common and standard XRD-based techniques for residual stress measurement.[17] Its widespread adoption is due in large part to its relative simplicity, ease of data processing, and non-destructive nature.[18] However, the method does have some limitations. For example, its accuracy can be affected by factors such as sample texture and grain size.[18] Additionally, for samples with complex geometries, the tilting of the sample can be restricted, potentially limiting the range of accessible ψ angles and thereby reducing the amount of data available for analysis.[19] Despite these drawbacks, the $\sin^2\psi$ method remains sufficiently robust for the purposes of this study.

Uncertainty in the XRD measurements is quantified using confidence interval: In AutoMATE II, confidence intervals for stress values measured by the XRD method are calculated using the t-distribution equation applied in linear regression. If ± ΔS represents the confidence interval of the stress value S, derived from the t distribution equation, ΔS can be calculated using the following equation:[20]

$$\Delta S = K \cdot t(\alpha, n-2)\sqrt{\frac{\Sigma[p_i - Mu_i + N)]^2}{(n-2)\Sigma(u_i - U)^2}} \quad (1)$$

where $t(\alpha,n\text{-}2)$ is the $100(1\text{–}\alpha)$ percentile of the t distribution with $(n-2)$ degrees of freedom. In AutoMATE II, the default value for α is 0.317 as recommended by the standard.[20] The variable K represents the stress constant, p_i is the measured peak positions, and n is the total number of p_i measurements. Furthermore, $u_i = \sin^2\psi_i$, while M and N are the slope and intercept, respectively, of the $\sin^2\psi$ plot obtained by the least square method. The term U is equal to $\Sigma u_i/n$, where Σ is the sum from $i = 1$ to n.

For the analysis of the results, stress values from the furthest points on the cross pattern from the ablation mark (4 mm from the center) served as reference points; the effects of laser ablation in these regions are presumed to be negligible. The residual stress measured at these reference points was employed as a baseline value to accurately assess the impact of the laser ablation on residual stress and served as the input for the initial residual stress in the simulation.

The diameter of the ablation mark measured around 1.6 mm. To achieve a high spatial resolution in the residual stress measurements, a 0.5 mm diameter collimator was utilized. The XDR measurements were performed in one direction (y-direction as

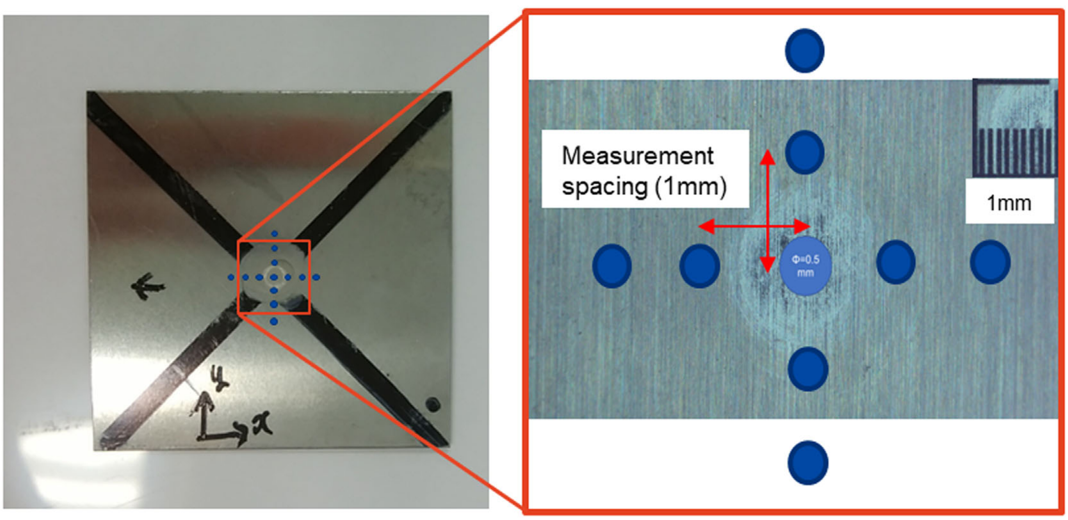

Figure 2. Laser-ablated SS316 specimen and the locations (blue dots) of the XRD residual stress measurements. Outermost dots are used as reference points for an area not affected by laser ablation.

shown in Figure 2) only. However, this effectively corresponds to two components of the stress: the radial direction (r) for points placed vertically and the tangential direction (ϕ) for points placed horizontally in Figure 2, if one uses a cylindrical coordinate system centered at the ablation spot.

3. Finite Element Model

Figure 3 illustrates the computational flow adopted in this study, highlighting the two-step approach to thermo-elastoplastic analysis performed in a weakly coupled manner (i.e., sequential solving approach). This process consists of two interconnected stages: a transient heat-transfer analysis followed by an elastoplastic stress analysis.

To simplify the model, several assumptions are made. The heat transfer adheres to Fourier's law. The laser's absorption depth is minimal, allowing it to be treated as surface heat flux. The melt pool size, formed by laser irradiation, is small enough to ignore convective flow. The ablation process is purely thermal, with material removal occurring solely through vaporization. Given the circular shape of the laser beam and the workpiece's relatively large size compared to the laser beam, the problem is simplified to being axis-symmetric.

Our previous study[21] found that convective heat transfer in nanosecond laser ablation has minimal impact on the temperature profile due to the small melt pool size and its short duration, justifying the neglect of convective effects in the thermal analysis. Additionally, the absorption depth of a 1064 nm laser in steel is only a few nanometers,[22] much smaller than the 250 μm material thickness, making the assumption of surface heat flux valid.

An axis-symmetric FEM model was developed using the general-purpose FEM software COMSOL v5.6. **Figure 4** illustrates the simulated geometry. The specimen thickness and laser parameters were the same for the model as in the experiment.

This model takes the laser parameters (laser pulse energy, wavelength, spot size, laser pulse spatial and temporal distribution, etc.) and material attributes (physical properties, geometry) as inputs, and predicts the residual stress magnitude and distribution as well as temporal and spatial variations of temperatures over an ablation process and ablation pit geometry.

Residual stress is greatly affected by temperature gradients.[23] To accurately evaluate residual stress, the target must first be stabilized near room temperature after laser ablation to alleviate thermal stresses. Therefore, an extended cooling phase was incorporated into the simulation, continuing until the surface temperature of the workpiece dropped to ≈10 K above ambient. Residual stresses were then assessed at the end of this cooling phase.

The simulations were conducted for a total of 0.2 s, reflecting three pulse sequences, each followed by an cooling phase. For each pulse, a large temperature gradient and significant heat input were expected during laser application and the period immediately after. Therefore, during the first 600 ns of each pulse, the maximum timestep was limited to 2 ns. Immediately following this ablation phase, a cooling period was modeled using a timestep of 1,000 ns. This pattern was repeated for all three pulses, ensuring a detailed representation of the ablation and subsequent cooling for each pulse. For the extended cooling

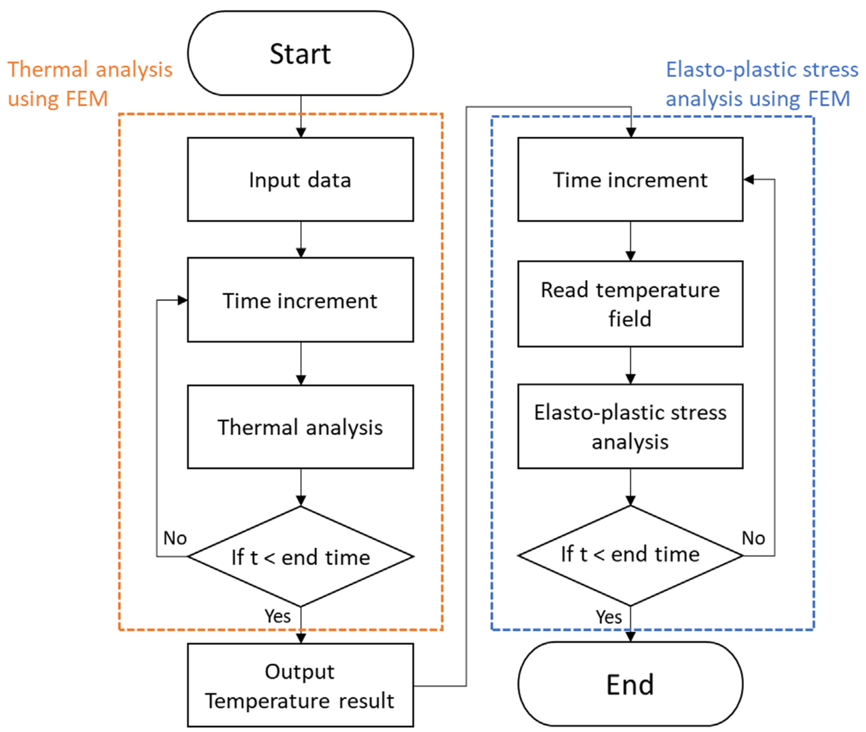

Figure 3. Flow chart of the thermally coupled elastoplastic FE analysis used in this model.

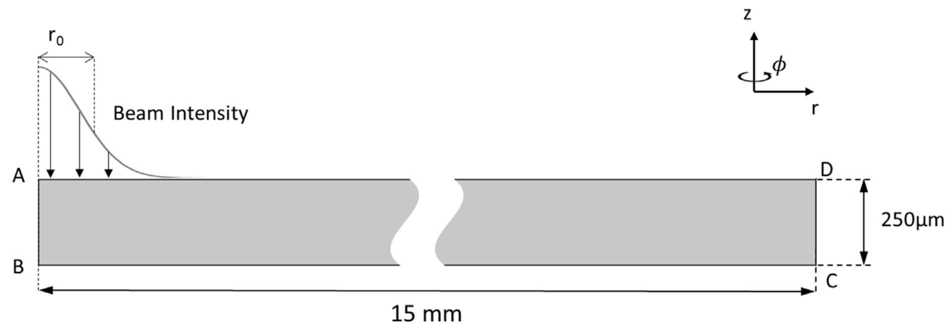

Figure 4. Simulated geometry for the nanosecond laser ablation spot on the SS316.

period after the final pulse, a larger timestep of up to 500 000 ns was adopted to efficiently capture extended cooling behavior.

3.1. Heat Transfer Model

In this simulation, the conduction and transport of the heat energy absorbed from a laser beam into the material is solved using equation (2):[24]

$$\rho C_p^{eq} \frac{\partial T}{\partial t} = \nabla \cdot (k \nabla T) + Q \tag{2}$$

where ρ is the mass density, T is the temperature, k is the thermal conductivity, and Q is the source/sink term. The term $C_p{}^{eq}$ represents the equivalent specific heat, with the superscript ^{eq} indicating that the latent heat of fusion is incorporated using the equivalent enthalpy approach.[25] As the material absorbs heat from laser irradiation, the phase change from solid to liquid is captured through the enthalpy change, with the latent heat of melting included as detailed in the equations below[25]:

$$C_p^{eq} = C_p + D_m L_m \tag{3}$$

where C_p represents the specific heat of the material without the inclusion of latent heat effects, L_m is the latent heat of fusion, and D_m is the Gaussian function normalized around the melting temperature T_m, given by

$$D_m = \frac{1}{\sqrt{2\pi}\Delta T} \exp\left(\frac{(T - T_m)^2}{\Delta T^2}\right) \tag{4}$$

where ΔT is the smoothing interval taken as the temperature range between the solidus and liquidus temperatures.

For the phase change from liquid to gas, the temperature recovery method[26] is used. It assumes that when a liquid temperature exceeds the boiling temperature, all the heat required to reach the temperature above the boiling temperature (T_v) is used for the phase change.

The temperature is then forced back to the boiling point by subtracting the amount of heat consumed by the vaporization (evaporative flux). The evaporation rate $\dot{m}$ is given by the following equation:

$$\dot{m} = \frac{q_v}{L_v} \tag{5}$$

where the evaporative flux q_v is given as:

$$q_v = h_a (T - T_v)(1 - \beta_r) \tag{6}$$

The retro-diffusion coefficient β_r is taken as 0.17,[27] indicating that 17% of the vaporized material re-condenses. h_a is a temperature-dependent heat-transfer coefficient that is zero for $T < T_v$ and increases linearly as $T > T_v$. The slope of this line is very steep, enforcing that the temperature of the solid cannot markedly exceed the ablation temperature.[28]

Ablation front movement is modeled by deforming the mesh geometry using an Arbitrary Lagrangian–Eulerian (ALE) moving mesh approach.[29] This method enables continuous surface evolution in response to laser energy input. As such, material removal is implicitly captured by mesh motion, with the corresponding mesh velocity $\overrightarrow{v_a}$ calculated as:

$$\overrightarrow{v_a} = \frac{\dot{m}}{\rho} \cdot \overrightarrow{n} \tag{7}$$

where $\dot{m}$ is the local mass removal rate, ρ is the material density, and $\overrightarrow{n}$ is the outward unit normal vector at the surface.

The material properties such as density, thermal conductivity, and specific heat capacities are considered a function of temperature in the FEM. These variable properties are calculated using a commercially available CALPHAD software, Thermo–Calc. **Figure 5** shows the calculated material of SS316. Additional parameters that are obtained from the literature are summarized in **Table 1** below.

The intensity of a laser beam when irradiated onto a substance is dictated by the Beer–Lambert law.[30] The beam intensity at a certain depth from the substance surface is represented by equation (8):

$$I(z) = I_0 (1 - R_{ref}) \exp(-\alpha z) \tag{8}$$

where R_{ref} symbolizes the surface reflectance of the laser beam; thus, (1-R_{ref}) represents the absorptivity of the material, while α denotes the extinction coefficient, which is the inverse of the characteristic depth at which the intensity of the absorbed laser beam decreases to 1/e of its initial value.

The absorption coefficient α can be calculated using the following equation:[30]

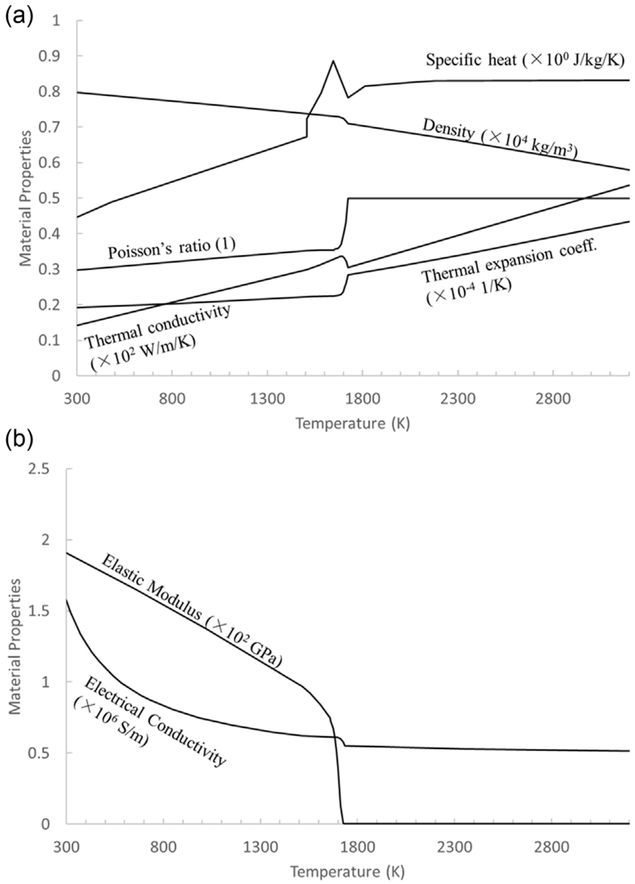

Figure 5. Material properties used in thermal elastoplastic FEM calculated using CALPHAD: a) specific heat, density, Poisson's ratio and thermal conductivity; b) elastic modulus and electrical conductivity.

Table 1. Additional material parameters used in the FEM simulation.

Material properties	Value
Absorption coefficient	Calculated using equation (10)
Ablation temperature (T_v)	3200 [K][44]
Latent heat of melting (L_m)	242.7 [kJ kg^{-1}][a)]
Latent heat of vaporization	6340 [kJ kg^{-1}][a)][45]
Average molar mass	55.187 [g mol^{-1}]

[a)]The value calculated by the CALPHAD method

$$\alpha = \frac{4\pi}{\lambda}\sqrt{\frac{\sigma}{2\omega\varepsilon_0}} \tag{9}$$

In this equation, λ represents the wavelength of the laser in meters, σ is the electrical conductivity of the material in $\Omega^{-1}\,\mathrm{m}^{-1}$, ω is the angular frequency of the laser in radians per second, and ε_0 is the permittivity of free space, $\approx 8.854 \times 10^{-12}\,\mathrm{F\,m^{-1}}$.[31]

Given the conditions of this study, the electrical conductivity of stainless steel used falls within the range of 0.5×10^6 to $1.5 \times 10^6\,\Omega^{-1}\,\mathrm{m}^{-1}$.[32] The laser angle frequency is within the range of 10^{14} to 10^{15} rad/s, which corresponds to a wavelength of 1,064 nm. This translates into an absorption depth on the order of tens to hundreds of nanometres. Since the domain size in this simulation is relatively large compared to the absorption depth, being 15 mm wide and 250 µm deep, the laser heat flux is applied as a boundary heat flux.

The absorption coefficient of laser light is influenced by its polarization and the angle of incidence onto the material surface. At normal angle of incidence, the target absorptivity is typically characterized in the following manner as per equation (10):[30]

$$(1 - R_{\mathrm{ref}}) = \sqrt{\frac{4\pi c\varepsilon_0}{\lambda\sigma}} \tag{10}$$

Although reflectivity may vary between the first and subsequent pulses due to surface modification during multi-pulse irradiation, a reflectivity based on equation (10) was consistently applied in this study for simplicity, and it was assumed that such variation is negligible.

The boundary conditions for the heat-transfer model are defined as follows: the boundary AB enforces axisymmetric conditions. The boundary AD is subjected to three conditions: incident laser flux representing laser irradiation, convective, and radiative heat flux. The remaining boundaries, BC and CD, are governed by radiative and convective boundaries.

Figure 7a illustrates the FEM model meshing employed for the heat-transfer analysis, featuring a mesh discretized with high spatial resolution focused toward the center of the laser spot, where a significant temperature gradient is anticipated. In these regions, elements sized smaller than 3 µm are utilized to accurately capture the ablation process. Consequently, the mesh designed for this analysis includes a total of 118,374 elements.

3.2. Elasto-Plastic Model

In laser ablation, the maximum strain rate can exceed $10^4\,\mathrm{s}^{-1}$ at a pulse duration in the nanosecond range,[33] while surface temperatures rise above 2000 K,[34] generating steep thermal gradients. These extreme conditions significantly affect the stress–strain response through a combination of strain-rate hardening and thermal softening. To account for these effects, the Johnson–Cook flow stress model[35] was adopted. The model captures strain hardening, strain-rate sensitivity, and thermal softening—including material weakening as temperatures approach melting—making it well-suited for high-rate, high-temperature applications such as laser ablation. It is also widely used in finite element simulations due to its relatively simple formulation and ease of integration into commercial solvers.[36]

The original Johnson–Cook model reduces material strength to zero at the melting point, T_m, leading to computational challenges, especially during laser ablation, where temperatures far exceed T_m. To address this, a minimal dummy strength, set at 2.5% of room temperature strength, is maintained beyond T_m to enhance solver stability. This adjustment is incorporated by modifying the temperature-dependent component of the Johnson–Cook equation, as detailed in equation (11):

$$\sigma_y = (A + B\varepsilon^n)\left(1 + C\ln\frac{\dot{\varepsilon}_p}{\dot{\varepsilon}_0}\right) \cdot \max\left(0.025, \left\{1 - \left(\frac{T - T_{ref}}{T_m - T_{ref}}\right)^m\right\}\right) \tag{11}$$

This modification ensures the strength is sustained even above the melting temperature, thus reducing the chance of numerical instability and premature termination of the solver. This is implemented by altering the built-in equations used to model the material's mechanical behavior. The parameters used for the Johnson–Cook model, as summarized in **Table 2**, are adopted from our previous study.[21]

There are three forces acting on the material surface during the ablation process: a recoil pressure caused by metal evaporation, surface tension forces arising from the liquid metal's inherent cohesive forces, and the Marangoni effect, which results from the gradient of surface tension along the surface caused by temperature or concentration variations. However, for nanosecond laser ablation, where the melt pool exists only for a few hundred nanoseconds and is extremely shallow, the latter two forces are considered negligible.

The recoil pressure is calculated based on the saturation pressure, outlined in equation (12), and incorporates the retro-diffusion coefficient, β_r.[37]

$$P_{rec} = P_{sat}\frac{(1 + \beta_r)}{2} \tag{12}$$

Here, saturation pressure P_{sat} is given by:

$$P_{sat} = P_0 \exp\left[\frac{ML_v}{R_g}\left(\frac{1}{T_v} - \frac{1}{T}\right)\right] \tag{13}$$

where P_0 is the reference pressure, 1 atm; L_ν is the latent heat of vaporization, and R_g is the ideal gas constant.

Initial residual stress was applied in the radial "r" direction as an initial condition of the model, reflecting experimental observations of surface residual stress prior to the laser ablation. This stress profile was defined as a symmetric parabolic distribution centered on the specimen's midline, consistent with the residual stress profile commonly observed in rolled steel thin sheets.[38] At both the top (0 μm) and bottom (250 μm) surfaces, the initial stresses are set at −125.6 MPa, denoting compression, while at the midpoint of the specimen (125 μm), the stress is set to + 60.5 MPa, indicating tension within the core. The implementation of these initial stress conditions is depicted in **Figure 6**.

When considering an averaging depth of XRD measurement from the top surface (taken as 30 μm in this study), these initial stresses produce an approximate average compressive stress of −85 MPa, which closely corresponds to the observed stress measurements obtained via XRD at the reference points. More details on the choice of averaging depth will be discussed in the results section of the paper.

Table 2. Johnson cook parameters for SS316 used in the simulations.

A [MPa]	B [MPa]	C	n	m	T_m [K]	T_{ref} [K]
342.4	932.0	0.275	0.0154	1.453	1697.8	293

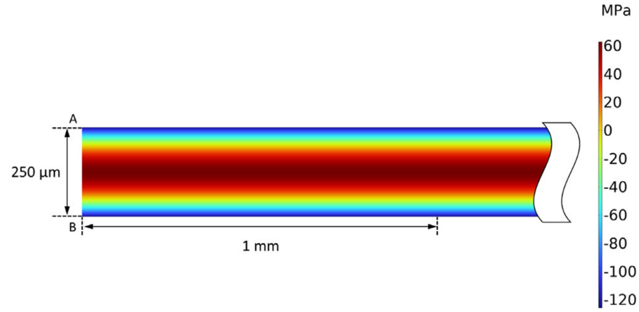

Figure 6. Initial residual stress induced in the simulated specimen.

The material properties related to the elasto-plastic model such as the elastic modulus, Poisson's ratio and thermal expansion coefficient are also considered a function of temperature in the FEM model in a similar manner as in the heat-transfer model.

The boundary conditions for the elasto-plastic model are defined as follows. The boundary AB enforces axis-symmetric conditions. On the boundary AD, a recoil pressure is applied to represent the ejection of the ablated material, and a deforming mesh boundary condition accounts for material removal due to laser ablation. Lastly, the boundary BC is set with roller support conditions to simulate support from the stage.

Figure 7b illustrates the FEM model meshing employed for this analysis. A thermal mesh convergence study was performed, with results validated against an analytical solution, confirming that the mesh is sufficient to capture the thermal phenomena accurately.

For the elasto-plastic stress analysis, a uniform mesh with an element size of ≈8 μm is employed, as indicated in Figure 6b, resulting in a total of 26 696 elements. This choice of mesh size is strategic, as using a smaller mesh than 8 μm would prematurely halt the solver due to stress singularity. It is also essential to note that the grain size of this steel ranges between 20 μm and 30 μm, and the objective of the modeling is to capture macroscopic residual stress (Type I) that spans multiple grains. Therefore, an 8 μm mesh size is deemed sufficient for both thermal and elasto-plastic stress analysis.

4. Results and Discussion

4.1. Experimental Results

Figure 8 illustrates the measured stress distribution for the ablated specimen. A tensile stress of 184 MPa is identified at the center of the ablation spot, which transitions to compressive stress as one moves radially outward. Compressive stresses ranging from approximately−75 to −100 MPa are observed at distances between 2 and 3 mm from the center. These values closely align with the reference point stress values within the measurement's error bars. Further out, at distances of 3 mm and 4 mm from the center, the measured stresses range from −70 to −90 MPa. These also fall within the error bars, suggesting that the effect of the laser ablation is localized to a 2 mm radius from the center.

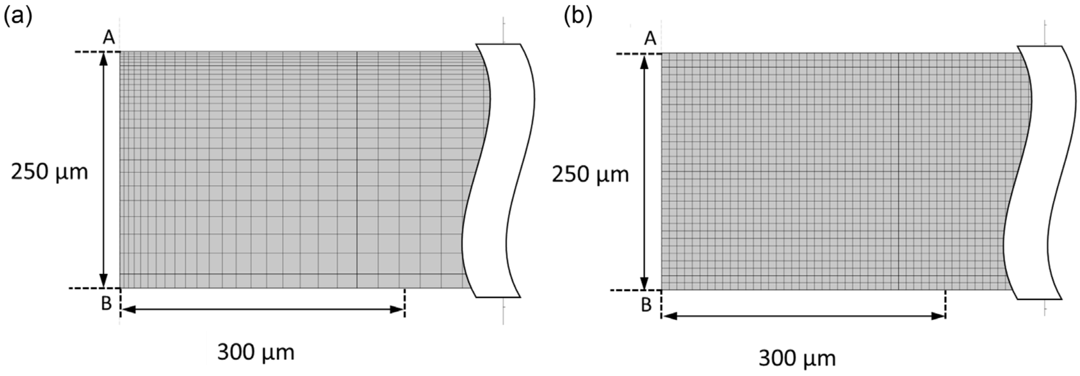

Figure 7. Mesh discretization for a) heat-transfer analysis, b) elasto-plastic stress analysis.

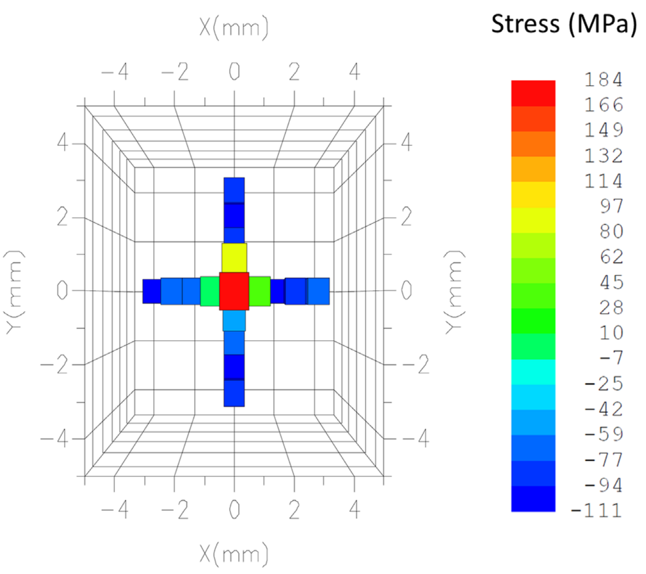

Figure 8. Planar representation of the residual stress distribution measured after laser ablation.

The results reveal no substantial difference in residual stress in the radial direction (σ_{rr} stress) and the tangential direction ($\sigma_{\phi\phi}$ stress), leading to the conclusion that the residual stress is approximately axis-symmetrical around the laser spot. In general, if the laser strikes as a perfect circle perpendicularly to the material surface, the stress distribution is considered to be axis-symmetric around the ablation center, as shown in these measurements.

4.2. Simulation

4.2.1. Model Validation

Figure 9a illustrates the transient maximum surface temperature when the laser is pulsed three times at 20 kHz. A distinct preheating effect from the previous pulses is evident, as indicated by the surface temperatures of 415 and 450 K before the second and third pulses, respectively. Additionally, the surface temperature measures 485 K at 150 000 ns, which occurs 50 000 ns after the third pulse, corresponding to the cooling interval between pulses. This represents temperature increases of 122 K after the first pulse and 35 K following each of the subsequent pulses, respectively.

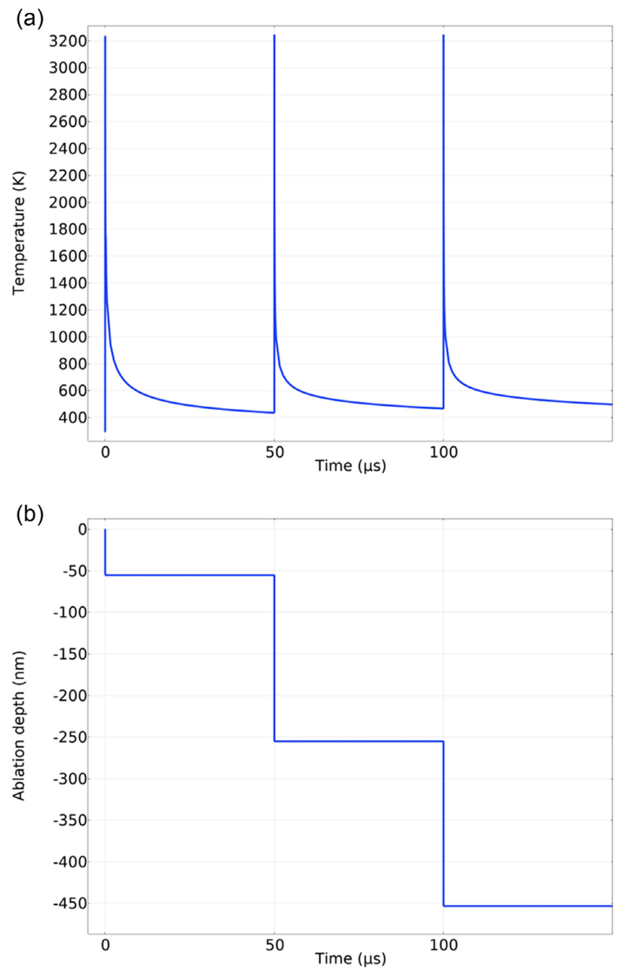

Figure 9. a) Maximum surface temperature variation with time when the laser is pulsed three times at 20 kHz at the same spot on the surface of the SS316 specimen. b) Ablation depth variation with time when the laser is pulsed three times at 20 kHz at the same spot on the surface of the SS316 specimen.

This difference can be attributed to the material's thermal inertia. In the initial pulse, the material starts from a lower, baseline temperature, allowing for a more significant temperature increase of 122 K. However, for the second and third pulses, the material is already "preheated" to temperatures of 415 K and 450 K, respectively. This preheated state reduces the margin for further temperature increase, resulting in a more moderate temperature change of 35 K for each of these subsequent pulses.

Figure 9b depicts the variation in ablation depth over time. As shown in Figure 9b, the first pulse ablates a smaller amount of material (removal depth of 155 nm) compared to the second pulse and third pulse (removal depth of 213 nm) This discrepancy can be attributed to the preheating effect, where the temperature increase of the material surface caused by the first and second pulses allows more energy to be used for ablation rather than heating. After the first pulse, the preheating temperature within the HAZ stabilizes, leading to similar ablation depths for subsequent pulses. The slight increase in the third pulse's ablation depth (220 nm) can be traced back to a marginally higher starting surface temperature resulting from the preheating effect.

The ablation profile is presented in **Figure 10**, showing an ablation pit size of ≈1 mm in the radial (r) direction and a depth of 600 nm in the vertical (z) direction.

The stress calculations were conducted based on the transient temperatures shown in Figure 9. During periods of significant temperature change, especially when the laser pulse was applied, the time steps were further divided into sub-steps. This ensured that the maximum temperature variation did not exceed 50 K within a single sub-step.

The residual stress tensor in the radial direction (r), tangential direction (ϕ), and vertical direction (z) calculated by the FEM models at the end of the 3-pulse ablation are shown in **Figure 11**a, b and c, respectively. By comparing Figure 11a,b, it can be said that the stress in the radial direction is very similar to that of the tangential direction, as expected from the axis-symmetric nature of this ablation process. Meanwhile, Figure 11c illustrates that the maximum residual stress in the vertical direction is ≈20 MPa. This value is significantly lower than that of the radial and tangential stresses, which can be attributed to the absence of any applied constraints in the vertical direction, as would be expected.

To validate the predicted thermal field, the simulated melt pool boundaries corresponding to the melting and vaporization thresholds were compared to the experimentally observed ablation crater, as shown in **Figure 12**. The isotherms for 1647 K (melting point) and 3200 K (vaporization threshold) are represented by green and red dashed lines, respectively. Extra care

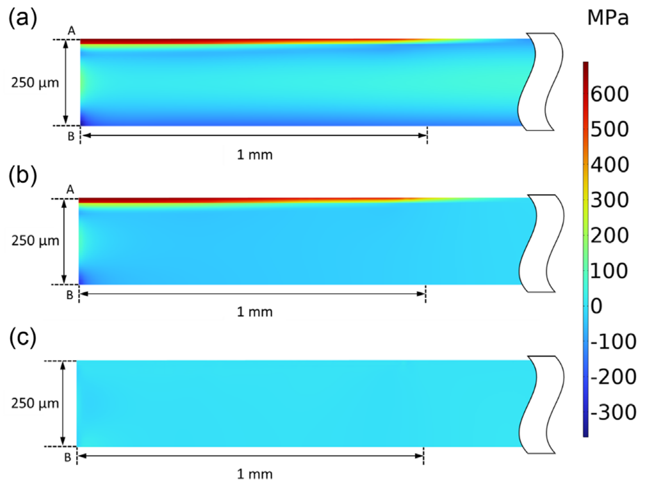

Figure 11. Residual stress in a) the radial (r), b) the tangential (φ), and c) the depth (z) directions, calculated by the FEM model at the end of the simulation. (The ablation profile is not visible in these plots due to its small depth (≈220 nm) relative to the domain size; an exaggerated view of the ablated geometry is shown in Figure 10).

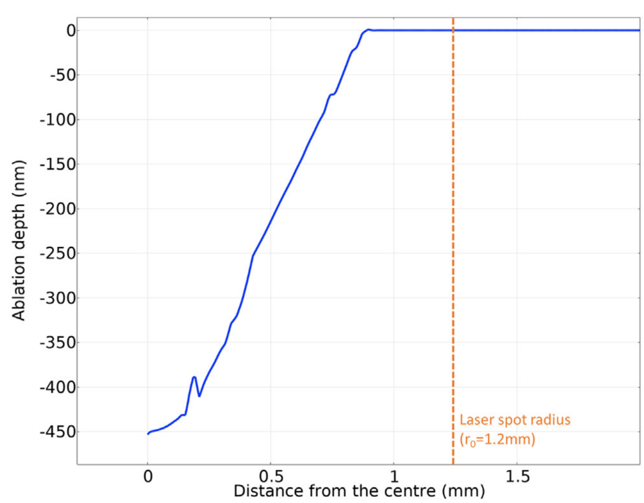

Figure 10. Exaggerated view of the ablated geometry at the end of the simulation (after three laser pulses), predicted using the FEM model.

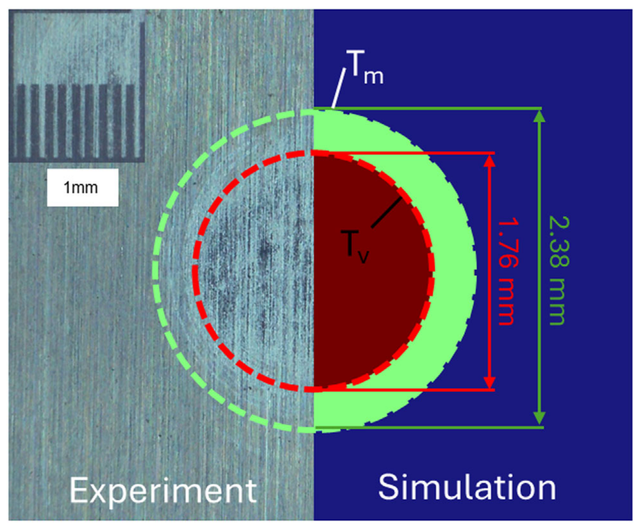

Figure 12. Validation of simulated temperature field via overlay of melting (T ≥ 1647 K) and vaporization (T ≥ 3200 K) contours on experimental crater image.

was taken to ensure consistent scale between the experimental and simulated images. The experimental image shows distinct zones: the central ablated area (shiny area), where material has been removed; a surrounding region where the surface morphology appears modified due to melting; and an outer unaffected region. The comparison indicates that the simulated vaporization region ($T \geq 3200$ K) corresponds well with the ablated area observed in the experiment, while the simulated melting region ($T \geq 1647$ K) aligns with the outer boundary of the surface modification zone. This agreement provides confidence in the accuracy of the predicted temperature field and confirms that the thermal model captures the key features of the laser–material interaction.

Figure 13a illustrates the residual stress distribution along the top surface of the specimen. From the figure, it can be said that the residual stress distribution extends ≈1.5 mm from the center of the laser, with the maximum radial component being 700 MPa in tension, substantially exceeding its yield strength of 340 MPa (at room temperature).

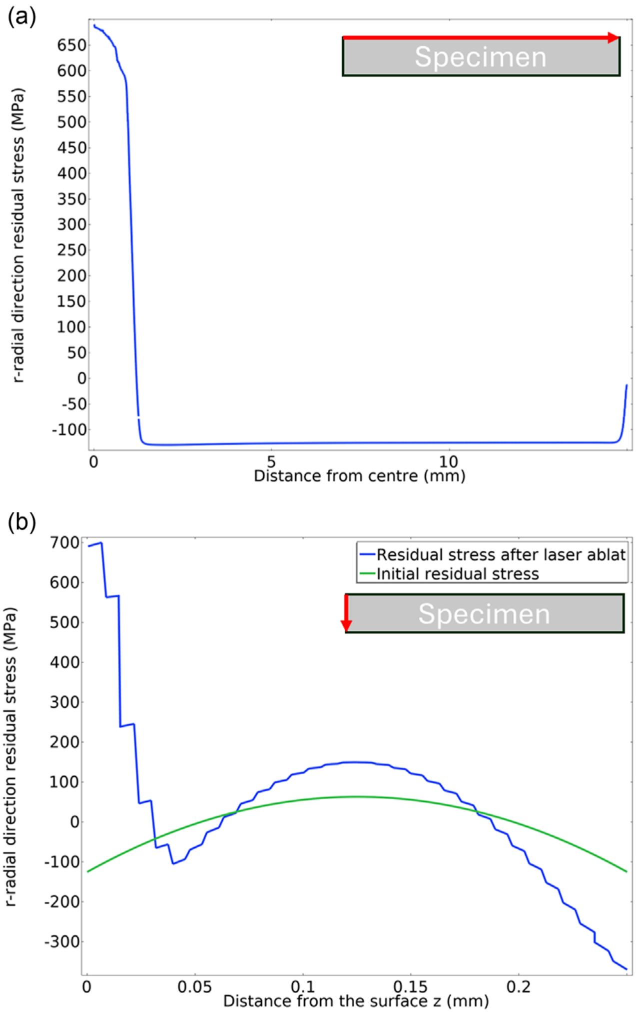

Figure 13. a) Residual stress distribution (rr component) along the top surface of the specimen, plotted along the red arrow, as predicted by the FEM model after 3-pulse ablation. b) Residual stress distribution (rr component) along the specimen thickness at the center of the ablation spot, also plotted along the red arrow the initial residual stress (green) and the post-ablation residual stress predicted by the FEM model (blue).

Figure 13b depicts the distribution of residual stress throughout the specimen's thickness, where the surface tensile stress of 700 MPa rapidly diminishes within the first 30 μm beneath the surface and transitions to a compressive stress, achieving a maximum compressive stress of −106 MPa at around 40 μm depth. The stress profile then reverses direction, moving back into tension, and reaches a secondary maximum tensile stress of 149 MPa at a depth of 124 μm. Deeper within the material, past 124 μm, the stress profile again reverses, declining in tensile stress and transitioning back into a compressive state around 187 μm, culminating in a compressive stress of −321 MPa at the rear of the specimen. This pattern shows that the substantial tensile stress near the surface of the material is counterbalanced by the development of larger and more intense compressive stress zones at the back of the specimen.

The comparison between the initial (green) and post-ablation (blue) residual stress along the specimen thickness is also shown in Figure 13b, illustrating the modification of the stress profile resulting from the laser ablation process. The process induces a substantial shift from an initial compressive stress of −126 MPa to a high tensile stress of 700 MPa at the surface, impacting the stress distribution throughout the material's cross-section. The ablation process not only increases the residual stress in magnitude but also widens the compressive zone. Post-ablation, the observed increase in compressive residual stress magnitude suggests an intensified counterbalancing effect within the material.

Figure 14 illustrates the evolution of the stress at the surface of the specimen at the center of the laser spot, providing insight into the residual stress formation during laser ablation. A significant tensile stress of nearly 700 MPa is observed at the surface after cooling; this can be explained by the following behavior. As the temperature rises in the laser-irradiated zone, the SS316 attempts to expand; however, the surrounding unaffected regions constrain this expansion. This results in an increase in the compressive stress in the laser-irradiated zone by the steep negative gradient in the first 100 ns, reaching a maximum compressive stress value of over −525 MPa.

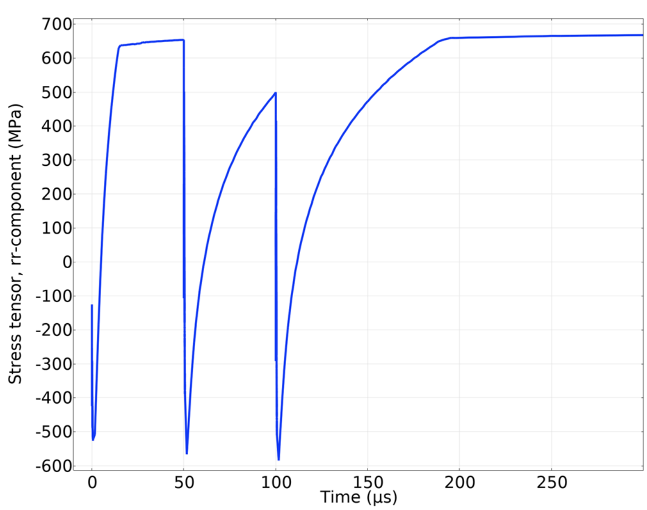

Figure 14. Evolution of the stress at the surface of the specimen at the center of the laser spot over the first 0–300 μs.

At a certain point, the stress in the surrounding non-heated region exceeds the material's yield point, leading to plastic deformation and making the deformation in those areas permanent. Once the laser irradiation ceases and the heated zone begins to cool and contract, the plastically deformed non-heated zone resists this contraction, resulting in the development of the tensile residual stress as depicted by the gradual increase in stress during cooling in Figure 14. This cycle is repeated with each of the three laser pulses.

Figure 15 presents a comparison between the residual stress values obtained experimentally and numerically according to their location relative to the center of the ablation spot. The residual stress at the back of the plate at the location of the ablation is also included.

The results of the FEM simulation align closely with the observed trends, where tensile stresses are found at the ablation center and compressive stresses manifest around the ablation spot. The experimental values were averaged over the four points equidistant from the center of the laser point.

To create an accurate and direct comparison between the numerical simulations and experimental measurements, the rr and $\phi\phi$ stress obtained in the simulations are averaged over an area of 0.55 mm radially and 30 μm in depth. This adjustment was made to account for the collimator diameter of 0.5 mm plus 10% divergence of the X-ray beam.

The depth of 30 μm was selected based on the X-ray penetration depth,[39] the selected depth corresponding to the sampling of 99% of the diffracted X-ray beam in stainless steel, as specified in the XRD device manufacturer's manual.

The analysis of Figure 15 raises several observations and explanations to consider. While the direction of the stress (either tensile or compressive) is consistently predicted by the model, discrepancies in magnitude are noteworthy.

At the center (0 mm) of the ablation spot, the FEM model significantly overestimates the stress, predicting 382.2 MPa compared to the experimental measurement of 183.9 ± 11.8 MPa. This discrepancy is likely attributable to the absence of crack formation in the FEM model. Specifically, the FEM model predicts maximum stress levels of well above the yield stress of the material at the laser spot center. In real-world situations, such elevated stress levels would typically instigate crack formations[4b] that act as stress relief mechanisms, reducing the maximum stress at the center, which the model fails to capture.

The overestimation has a cascading effect on adjacent points, influencing the stress prediction at 1 mm from the center and on the back of the specimen. Specifically, at 1 mm from the center, the simulation predicts a residual stress of 51.9 MPa, which is slightly higher than the experimental value of 21.0 ± 21.2 MPa. Furthermore, the exaggerated stress on the front side consequently influences stress calculations on the rear side, as increased front-side tensile stress would also proportionally increase rear-side compression, due to the counterbalancing effect.

Moving away from this high-stress central region, at distances of 2 mm, 3 mm, and 4 mm away from the center, the effects of laser ablation diminish. In these regions, the measured residual stress predominantly reflects pre-existing residual stress, lending credence to the model's ability to correctly predict the spatial impact of laser ablation on residual stress and thereby validating its close agreement with experimental data.

Figure 15 demonstrates that both the simulation and experimental results exhibit a similar trend, with the exception of a steeper stress gradient between 0 and 1 mm in the simulation. This congruence suggests that the simulation, albeit not numerically exact, provides a correct model for capturing residual stress characteristics in the material. A refined model accounting for stress-relieving phenomena would likely result in stress predictions aligning more closely with experimental data.

Other sources of discrepancy can be attributed to variations in material properties. Specifically, the Johnson–Cook parameters for the simulation were obtained from our previous study. However, these properties might be different for the SS316 plate tested in the experiment. It is worth emphasizing that if actual experiments were conducted to determine the material parameters, the accuracy of the simulation results could be further improved.

This result highlights the model's significant potential for various industrial applications, particularly in laser cleaning processes, where maintaining stress levels below the cracking

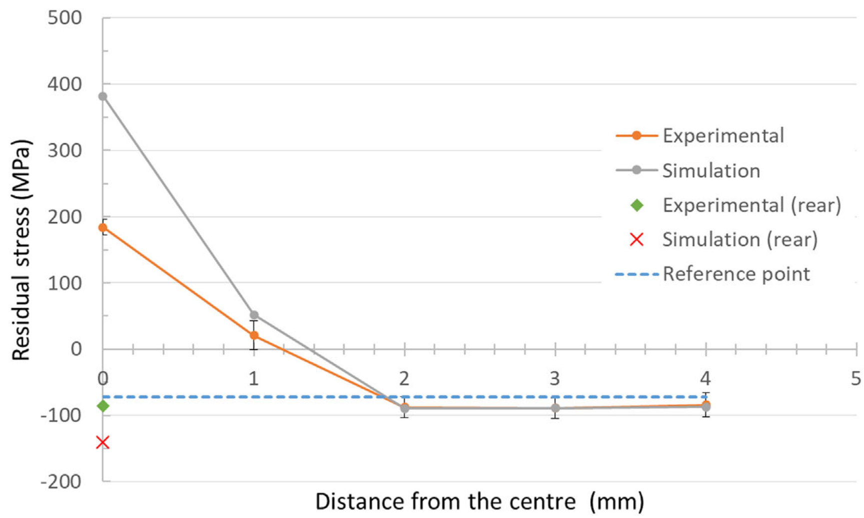

Figure 15. Comparison of experimental versus simulated residual stress distribution of laser-ablated SS316 steel.

threshold is critical. The comparison between experimental and simulation results demonstrates strong alignment in capturing the residual stress directions and its spatial extent, validating the model's ability to predict key stress trends. However, discrepancies exist, particularly in peak stress magnitudes at the ablation center, where the model overestimates tensile stress due to the absence of stress-relieving mechanisms such as crack formation. Additionally, variations in material properties between the simulation and experiment may contribute to these differences. While the model provides reasonable accuracy for stress predictions in conditions devoid of cracking, its precision may diminish in high-stress regions where cracking occurs.

Despite this limitation, the model remains an effective tool for industrial applications that operate within safe stress margins, making it a valuable tool for optimizing laser ablation processes while mitigating the risk of material failure.

4.2.2. Parametric Study

The parametric study was performed using the FEM model validated in the previous section. However, to more clearly isolate the effects being studied, the initial conditions have been modified to remove any pre-existing residual stress, resulting in a stress-free material at the onset. The study is conducted to investigate the specific effects of these parameters on the development of residual stress in the material.

First, the effect of fluence on residual stress is investigated. For this analysis, the experiment was conducted with a single pulse, and the pulse energy was varied: 0.15 J, 0.0692 J, 0.0472 J, and 0.0225 J, achieving fluences of 3.4 J cm^{-2}, 1.57 J cm^{-2}, 1.07 J cm^{-2}, and 0.51 J/cm^{-2}, respectively. Other laser parameters, such as wavelength and spot diameter, were kept constant throughout the parametric study. These selected fluences cover key temperature thresholds, such as ablation and melting points for this particular material.

Figure 16 illustrates the transient maximum surface temperatures corresponding to these different fluences. As expected, the maximum temperature decreases as the fluence decreases. Specifically, 3.4 J cm^{-2} corresponds to a maximum temperature of 3236 K, which is above the ablation threshold; 1.57 J cm^{-2} corresponds to 1934 K, which is above the melting point; and the temperatures reached for 1.07 J cm^{-2}, 0.77 J cm^{-2}, and 0.51 J cm^{-2} are below the melting point.

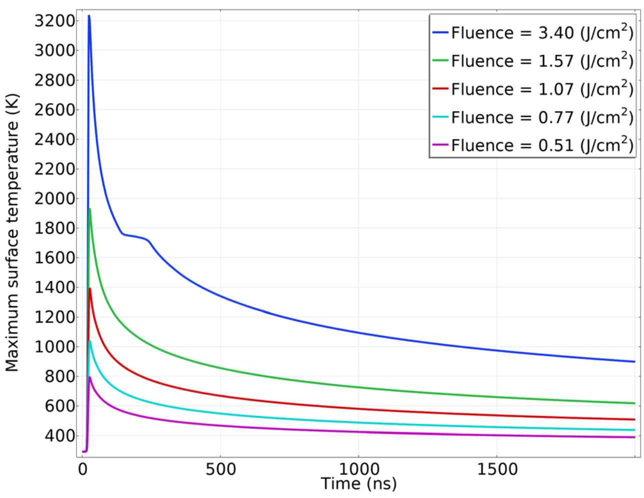

Figure 16. Detailed view of the maximum surface temperature variation with time for different laser fluences for 0–2000 ns of the simulation.

Figure 17a illustrates the surface residual stress for various fluence levels, while Figure 17b shows the residual stress distribution along the depth of the material. From these figures, it is evident that higher fluences result in increased residual stress. The increase in residual stress is directly linked to the rise in surface temperature, which instigates more pronounced thermal expansion in the material, thereby inducing greater thermal stress during the process of laser ablation. Furthermore, the figures also indicate that at higher fluences, not only does the residual stress magnitude increase, but also the stress profile extends to a wider region in the material, both in width and depth. This wider distribution of residual stress is the result of a larger HAZ at higher fluences, as well as the need for a wider balancing zone

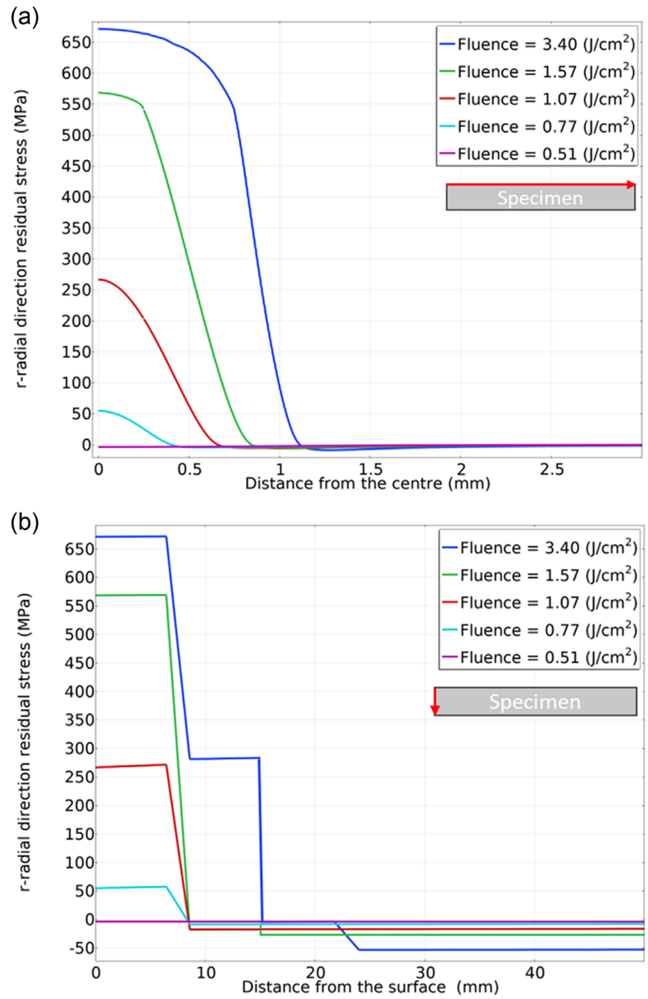

Figure 17. a) Residual stress distribution along the top surface of the specimen for different fluences (stress tensor rr component). b) Residual stress distribution along the thickness of the specimen at the center of the ablation spot for different fluences (stress tensor rr component).

to maintain the material's internal equilibrium against the elevated residual stress levels.

The relationship between maximum surface temperatures and residual stress is more relevant for our discussion than the influence of the fluence. As illustrated in **Figure 18**, a direct correlation exists between these two variables, for maximum temperatures ranging between 1934 K and 3236 K; temperatures both above the melting temperature of SS316, the variation in residual stress observed is relatively small. Specifically, the maximum tensile stress recorded falls within a narrow band between 568 and 671 MPa. This rather small variation is attributed to the substantial decrease in the material's stiffness upon melting. In its molten state, the reduced stiffness of the material means it cannot exert as much stress on the surrounding areas. This reduction in the material's ability to push against adjacent confined regions explains the plateau in residual stress, despite further temperature increases.

For maximum surface temperatures between 1042 K and 1934 K, the temperatures below the ablation spot mostly fall below the melting point of SS316. For this maximum temperature range, a linear correlation between maximum surface temperature and residual stress is noted. Specifically, a maximum surface temperature of 1934 K generates a maximum residual stress of 267 MPa, while a maximum surface temperature of 1042 K yields a maximum residual stress of 55 MPa.

At the lowest fluence of 0.51 J cm^{-2}, the thermal expansion of the material is entirely elastic, making it possible to achieve zero residual stress in the material. The data point at 0.51 J cm^{-2} does not follow the linear trend observed with higher fluences, suggesting it is below the threshold for residual stress formation. This threshold is represented by a point on the graph indicating the onset of residual stress, which can be estimated through linear extrapolation of the data in the linear region (illustrated by the orange dashed line). In this instance, the extrapolation suggests that the threshold temperature for residual stress formation is ≈940 K.

In the subsequent phase of the parametric study, the focus is on assessing the impact of pulse duration on residual stress. It has been established from previous studies that increasing the

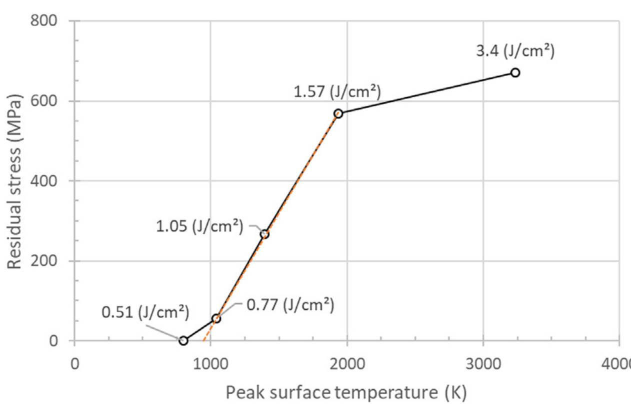

Figure 18. Relationship between maximum surface temperature and maximum residual stress value after single-pulse laser ablation. The orange dashed line represents the linear extrapolation used to calculate the threshold value of the maximum surface temperature that will result in residual stress formation.

pulse duration results in a lower maximum surface temperature, which leads to reduced residual stress. To accurately evaluate the effects of varying pulse durations, it is essential to control for temperature variations, ensuring that the maximum surface temperatures remain consistent across different pulse durations.

To rectify this and to accurately study the influence of pulse duration on residual stress distribution, a parametric study was designed. This study adjusted the pulse duration and fluence simultaneously, ensuring the maximum surface temperature remained constant across the tested cases. This is calculated as follows:

The maximum temperature at the center of a single-spot circular laser pulse can be treated as a one-dimensional heat conduction problem, assuming a semi-infinite object with a uniform initial temperature, $T = T_0$. At time $t = 0$, the object is subjected to a constant heat flux q_0 for the duration τ_p (pulse duration).

Ignoring the convective heat transfer within the melt pool, the differential equation - equation (14) for determining the temperature distribution of a semi-infinite object at a specific time t can be written using the Fourier law:[40]

$$\frac{\partial T}{\partial t} = \alpha \frac{\partial^2 T}{\partial x^2} \tag{14}$$

where α is the thermal diffusivity given as $k/\rho C_p$.

The initial and boundary conditions are given by equation (15) to equation (17).

$$T = T_0 \quad \text{at} = 0\ \forall\ x \quad \text{Initial condition} \tag{15}$$

$$T = T_0 \quad \text{at x} = \infty\ \forall\ \text{t} \quad \text{Constant temperature at the infinite end} \tag{16}$$

$$-k\frac{\partial T(0,t)}{\partial x} = I_a \quad \text{at x} = 0\ \&\ \text{t} > 0. \quad \text{Prescribed heat flux at the irradiated surface} \tag{17}$$

Here, I_a is an absorbed laser heat flux defined as $I_a = (1\text{-}R_{ref})\cdot I_0$, with I_0 being the incident laser heat flux.

The solution for the differential equation with such a boundary condition is given by equation (18):[41]

$$T - T_0 = \frac{I_a}{k}\left[\frac{\sqrt{4\alpha t}}{\sqrt{\pi}} e^{(-x^2/4\alpha t)} - x\text{erfc}\left(\frac{x}{\sqrt{4\alpha t}}\right)\right] \tag{18}$$

Assuming the laser heat flux is much greater than the conduction flux near the surface, $I_a \gg k\frac{\partial T}{\partial x}$ and the radiative and convective heat losses are negligible compared to the absorbed incident flux, the maximum temperature occurs at $x = 0$ and $t = \tau_p$. Therefore equation (18) can be integrated from 0 to τ_p to find the temperature at the surface at the end of the pulse, as per equation (19)

$$T - T_0 = \int_0^{\tau_p} \frac{I_a}{k}\frac{\sqrt{4\alpha t}}{\sqrt{\pi}} dt \tag{19}$$

The above equation simplifies as follows in equation (20):

$$T - T_0 = \Delta T_{max} = C_1 \frac{F_a}{t_p}\left(\frac{\sqrt{4\tau_p}}{\sqrt{\pi \rho C_p k}}\right) \tag{20}$$

where $F_{\alpha} = (1\text{-}R)F$ is the absorbed fluence, R the material reflectivity, and C_1 an integration constant calculated by integrating the laser excitation (I_a) over the duration of the pulse (i.e., varying intensity over time). For a Gaussian excitation pulse, $C_1 = 0.783$.[42]

Utilizing equation (20), it is observed that as pulse duration increases, the maximum temperature decreases. To maintain the same maximum temperature, the fluence must be increased accordingly. This can be achieved either by increasing the pulse energy while keeping the spot size constant, or by reducing the spot size while keeping the pulse energy constant. In this study, adjustments were made using the former approach by increasing the pulse energy.

Table 3 outlines the tested combinations of fluence (F) and pulse duration (τ_p), all configured to achieve identical maximum surface temperatures by adjusting the pulse energy while keeping the surface area consistent. The selected pulse duration range, from 5 ns to 100 ns, spans a broad spectrum within the nanosecond laser regime. While 5 ns represents the lower end for nanosecond lasers and some lasers can have pulse durations exceeding 100 ns, this range already covers a sufficiently large variation. As shown in the results, this selection allows for clear trend identification and is sufficient for drawing meaningful conclusions in this study.

Figure 19 illustrates the transient maximum surface temperature for different fluences and pulse durations. As it can be seen in the graph, for all combinations of fluence and pulse duration, the same maximum temperature of 3200 K is reached, as we had aimed for. The major difference is the shape of the curves; longer pulse duration results in a more horizontally stretched-out shape as the heat is applied over a longer time period.

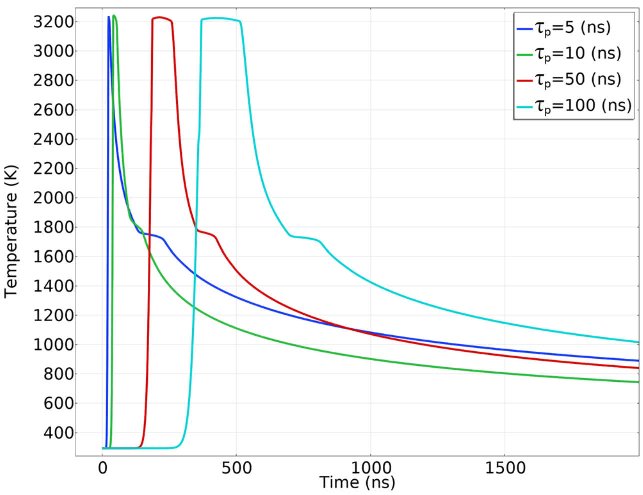

Figure 19. Detailed view of the maximum surface temperature variation with time for different laser pulse durations (0–2,000 ns).

Table 3. Combinations of pulse duration (τ_p) and fluence (F) tested for a constant maximum surface temperature.

τ_p [ns]	F [J cm^{-2}]
5	3.40
10	4.81
50	10.75
100	15.21

The resultant residual stress distributions are presented in **Figure 20** a,b. From the observed patterns, it becomes clear that as the pulse duration increases, the residual stress distribution curve widens while retaining a similar overall shape; the same is true for the thickness direction. Interestingly, despite the variations in pulse duration and fluence, the maximum residual stress does not change significantly across the different scenarios, ranging between 620 MPa and 680 MPa. This observation highlights a critical insight into the relationship between fluence, pulse duration, and residual stress. By combining the findings from the fluence parametric study, it becomes evident that the maximum temperature governs the maximum residual stress, while the pulse duration influences the spatial extent or area affected by this stress. By keeping the maximum temperature

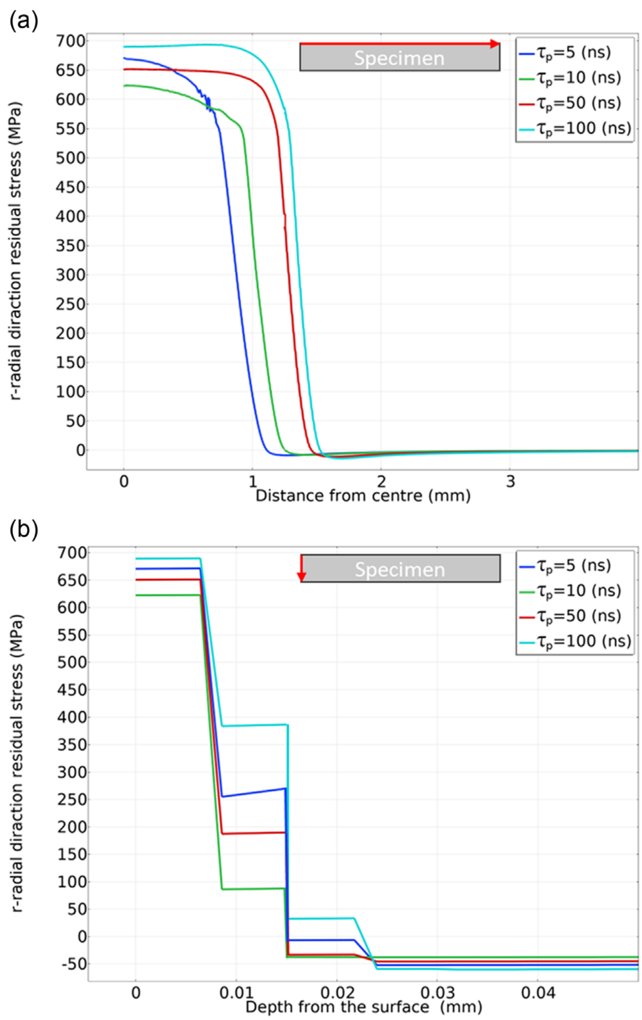

Figure 20. a) Residual stress distribution along the top surface of the specimen for different pulse durations (stress tensor rr component). b) Residual stress distribution along the thickness of the specimen at the center of the ablation spot for different pulse durations (stress tensor rr component).

ADVANCED ENGINEERING MATERIALS
www.aem-journal.com

constant, the maximum residual stress levels show minor variation, while adjustments in pulse duration create variations in the stress distribution's width and depth.

This phenomenon can be explained by considering the thermal dynamics at play. When considering heat dissipation in an isotropic material during laser heating, the laser can be considered as a point heat source on the surface of the material. The heat will dissipate from the source evenly in every direction, forming a spherical shape of heat flux. The thermal diffusion length L_D[43] is given by equation (21):

$$L_D = \sqrt{Dt} \tag{21}$$

where D is the thermal diffusivity defined as $k/\rho C_p$.

As the heat is applied over a more extended period, more thermal energy dissipates from the surface to the bulk of the material, causing the entire curve to spread out. However, since the shape of the distribution is primarily dictated by the maximum temperature, the general form does not change significantly. If the bulk material is sufficiently large, that is, the overall bulk temperature does not change significantly, changing pulse duration enlarges L_D. This is equivalent to enlarging and shrinking the thermal profile by the square root of τ_p.

5. Conclusion

This study presents a comprehensive investigation into the prediction of residual stress, emphasizing the robustness and accuracy of the numerical simulations and yielding several significant findings. 1) One of the most compelling outcomes is drawn from the FEM model demonstrating strong capabilities in predicting residual stress trends. While the model accurately predicted the direction of stress, some discrepancies in magnitude were noted. These were mainly due to the model's limitation in not accounting for crack formation, especially at the center of the ablation spot. Despite this, the model closely aligned with experimental data at distances away from the high-stress zone, validating its overall reliability; 2) Another critical insight derived from this study is the strong influence of maximum temperature on residual stress. The correlation is categorized mainly into three regions. First, below the threshold temperature for residual stress formation, where thermal stress is entirely elastic, resulting in no residual stress after the laser ablation. Second, in the linear region above this threshold temperature but below the melting point, there is a linear correlation between maximum surface temperature and residual stress. Finally, above the melting point, residual stress plateaus because, upon melting, the material's ability to impose stress on adjacent confined areas is significantly reduced due to a substantial reduction in the material's stiffness. This connection between temperature and stress enables the understanding and control of the thermal effects in laser processing and 3) further key observations center on the effects of pulse duration and fluence on residual stress distribution. The parametric study revealed that lower fluence results in lower residual stress, while increasing pulse duration widens the residual stress distribution curve in both width and depth, yet the overall shape remains similar. Interestingly, when pulse duration and fluence are varied simultaneously to maintain the same peak temperature, the maximum residual stress remains relatively consistent. This highlights a critical relationship between fluence, pulse duration, and residual stress, where maximum temperature governs the maximum residual stress, and pulse duration determines the spatial extent or area affected.

Acknowledgements

The authors acknowledge the contribution of Dr Wen Hao Kan and Monash University for providing access to Thermocalc software and running the simulations to obtain the variations of properties with temperature for the five materials investigated here. This research was undertaken with the assistance of resources from the National Computational Infrastructure (NCI Australia), an NCRIS enabled capability supported by the Australian Government. Yutaka Tsumura acknowledges sincere gratitude to ANSTO for their invaluable technical and financial assistance, made possible through the ANSTO FutureNow Scholarship. This research was supported by the Australian Government through the Australian Research Council's Linkage Project funding scheme (Project LP180100276) and Transport for NSW, Australia.

Open access publishing facilitated by The University of Sydney, as part of the Wiley - The University of Sydney agreement via the Council of Australian University Librarians.

Conflict of Interest

The authors declare no conflict of interest.

Author Contributions

Yutaka Tsumura: conceptualization (lead); data curation (lead); formal analysis (lead); investigation (lead); methodology (lead); validation (lead); writing—original draft (lead); writing—review & editing (equal). **Anna Paradowska**: funding acquisition (equal); project administration (equal); supervision (equal); writing—review & editing (equal). **Andrei V. Rode**: funding acquisition (equal); project administration (equal); writing—review & editing (equal). **Steve Madden**: funding acquisition (equal); project administration (equal); writing—review & editing (equal). **Ludovic Rapp**: writing—review & editing (equal). **Meera Mohan**: writing—review & editing (equal). **Alison Wain**: resources (equal); writing—review & editing (equal). **Gwénaëlle Proust**: funding acquisition (equal); project administration (equal); supervision (equal); writing—review & editing (equal).

Data Availability Statement

The data that support the findings of this study are available from the corresponding author upon reasonable request.

Keywords

Laser ablation, numerical simulation, residual stress, X-ray diffraction

Received: February 20, 2025
Revised: June 22, 2025
Published online: July 16, 2025

[1] C. Dowding, A. Borman, *Laser Surface Engineering*, **2015**, Elsevier, p. 523.
[2] J. Zhang, D. Yang, A. Rosenkranz, J. Zhang, L. Zhao, C. Song, Y. Yan, T. Sun, *Adv. Eng. Mater.* **2019**, *21*, 1801016.

[3] N. Ahmed, S. Darwish, A. M. Alahmari, *Mater. Manuf. Processes* **2016**, *31*, 1121.
[4] a) Y. Seo, S. Son, D. Lee, *Mater. Chem. Phys.* **2022**, *288*, 126375; b) M. Shamsujjoha, S. R. Agnew, M. A. Melia, J. R. Brooks, T. J. Tyler, J. M. Fitz-Gerald, *Surf. Coat. Technol.* **2015**, *281*, 193.
[5] M. Hino, Y. Hashimoto, Y. Mitooka, *J. Surf. Finish. Soc. Jpn.* **2018**, *69*, 435.
[6] P. Withers, *Rep. Prog. Phys.* **2007**, *70*, 2211.
[7] a) H. Büttner, K. Michael, J. Gysel, P. Gugger, S. Saurenmann, G. de Bortoli, J. Stirnimann, K. Wegener, *J. Mater. Process. Technol.* **2020**, *285*, 116766; b) B. Liu, G. Mi, C. Wang, *Mater. Chem. Phys.* **2020**, *255*, 123500.
[8] N. Maharjan, W. Zhou, Y. Zhou, Y. Guan, N. Wu, *Surf. Coat. Technol.* **2019**, *366*, 311.
[9] B. Yilbas, S. Shuja, A. Arif, M. Gondal, *J. Mater. Proc. Technol.* **2003**, *135*, 6.
[10] a) B. Denkena, B. Breidenstein, L. Wagner, M. Wollmann, M. Mhaede, *Int. J.Refract. Met. Hard Mater.* **2013**, *36*, 85; b) M. Shamsujjoha, S. R. Agnew, J. R. Brooks, T. J. Tyler, J. M. Fitz-Gerald, *Surf. Coat. Technol.* **2015**, *281*, 206.
[11] J. Zhang, S. Zhang, G. Chen, Z. Jia, Y. Qu, Z. Guo, *Int. J. Mech. Sci.* **2022**, *230*, 107528.
[12] a) K.-H. Leitz, B. Redlingshöfer, Y. Reg, A. Otto, M. Schmidt, Physics Procedia **2011**, *12*, 230; b) Z. Liao, A. la Monaca, J. Murray, A. Speidel, D. Ushmaev, A. Clare, D. Axinte, R. M'Saoubi, *Int. J. Machine Tools and Manuf.* **2021**, *162*, 103687.
[13] P. S. Prevey, *ASM Handbook, Vol. 10: Materials Characterization*, (Ed: A. S. M. International), ASM International, Materials Park, OH **1986**. 380.
[14] A. Allen, M. Hutchings, C. Windsor, C. Andreani, *Adv. Phys.* **1985**, *34*, 445.
[15] a) G. Zhu, S. Wang, W. Cheng, G. Wang, W. Liu, Y. Ren, *Coatings* **2019**, *9*, 578; b) Y. Jiao, E. Brousseau, K. Kosai, A. J. Lunt, J. Yan, Q. Han, H. Zhu, S. Bigot, W. He, *Mater. Sci. Eng.: A* **2021**, *803*, 140497.
[16] a) J. J. Zhang, L. Zhao, A. Rosenkranz, C. W. Song, Y. D. Yan, T. Sun, *Adv. Eng. Mater.* **2019**, *21*, 1900193; b) H. S. Lim, J. Yoo, *J. Mech. Sci. Technol.* **2011**, *25*, 1811; c) J. Lee, J. Yoo, K. Lee, *J. Mech. Sci. Technol.* **2014**, *28*, 1797.
[17] C. Balasingh, A. Singh, *Met., Mater. Processes* **2000**, *12*, 269.
[18] A. Lodh, K. Thool, I. Samajdar, *Trans. Indian Inst. Met.* **2022**, *75*, 983.
[19] A. Sarmast, J. Schubnell, J. Preußner, M. Hinterstein, E. Carl, *J. Mater. Sci.* **2023**, *58*, 16905.
[20] The Committee on X-ray Study of Mechanical Behavior of Materials in the Society of Materials Science, *Standard Method For X-ray Stress Measurement (JSMS-SD-10-05)*; The Society of Materials Science: Kyoto, Japan, **2005**.
[21] Y. Tsumura, *Numerical Insights Into Laser Ablation: A Pathway To Optimised Steel Cleaning For The Sydney Harbour Bridge*, Ph.D. thesis, The University of Sydney, Sydney **2024**.
[22] Z. Yang, A. Bauereiß, M. Markl, C. Körner, *Adv. Eng. Mater.* **2021**, *23*, 2100137.
[23] D. Radaj, *Heat effects of welding: Temperature field, residual stress, distortion*, Springer Science & Business Media **2012**.
[24] J. Ahn, E. He, L. Chen, T. Pirling, J. Dear, C. Davies, *Mater. Sci. Eng.: A* **2018**, *712*, 685.
[25] X. Fan, G. Qin, Z. Jiang, H. Wang, *J. Mater. Res. Technol.* **2023**, *22*, 2549.
[26] T. Tszeng, Y.-T. Im, S. Kobayashi, *Int. J. Mach. Tools and Manuf.* **1989**, *29*, 107.
[27] A. Queva, G. Guillemot, C. Moriconi, C. Metton, M. Bellet, *Addit. Manuf.* **2020**, *35*, 101249.
[28] W. Frei, *Modeling Thermal Ablation For Material Removal*, COMSOL **2023**. [Online]. Available: https://www.comsol.com/blogs/modeling-thermal-ablation-for-material-removal
[29] J. Donea, A. Huerta, J.-P. Ponthot, A. Rodríguez-Ferran, *In Encyclopedia of Computational Mechanics*, Vol. *1*, John Wiley & Sons Ltd, Chichester, UK **2004**, Chap. 14. 413
[30] L. Li, D. Zhang, Z. Li, L. Guan, X. Tan, R. Fang, D. Hu, G. Liu, *Phys. B* **2006**, *383*, 194.
[31] W.-I. Cho, S.-J. Na, C. Thomy, F. Vollertsen, *J. Mater. Proc. Technol.* **2012**, *212*, 262.
[32] J. Matolich Jr., *Thermal Conductivity and Electrical Resistivity of Type 316 Stainless Steel from 0 to 1800°F*, NASA-CR-54151; BATT-7096, National Aeronautics and Space Administration, Washington, D.C., **1965**.
[33] a) J. Radziejewska, *Opt. Laser Technol.* **2016**, *78*, 125; b) W. Moćko, J. Radziejewska, A. Sarzyński, M. Strzelec, J. Marczak, *Opt. Laser Technol.* **2017**, *90*, 165.
[34] M. Dal, L. Carvalho, A. Semerok, W. Pacquentin, H. Maskrot, *In Proc. COMSOL Conference 2019*, COMSOL, Burlington, MA, USA **2019**. [Online]. Available: https://www.comsol.com/paper/simulation-of-bi-material-nano-second-laser-ablation-82861
[35] G. R. Johnson, W. H. Cook, *In Seventh International Symposium on Ballistics: Proceedings*, American Defense Preparedness Association **1983**, p. 541.
[36] A. Priyadarshini, S. K. Pal, A. K. Samantaray, *J. Mach. Form. Technol.* **2012**, *4*, 59.
[37] L. L. Beghini, M. Stender, D. Moser, B. L. Trembacki, M. G. Veilleux, K. R. Ford, *Comput. Mech.* **2021**, *67*, 1041.
[38] R. Nakhoul, P. Montmitonnet, M. Potier-Ferry, *Int. J. Solids Struct.* **2015**, *66*, 62.
[39] Y. Javadi, M. Smith, K. A. Venkata, N. Naveed, A. Forsey, J. Francis, R. Ainsworth, C. Truman, D. Smith, F. Hosseinzadeh, *Int. J. Pressure Vessels Piping* **2017**, *154*, 41.
[40] B. N. Chichkov, C. Momma, S. Nolte, F. Von Alvensleben, A. Tünnermann, *Appl. Phys. A* **1996**, *63*, 109.
[41] J.-C. Han, L. M. Wright, *Analytical Heat Transfer*, Taylor & Francis **2022**.
[42] E. Besozzi, A. Maffini, D. Dellasega, V. Russo, A. Facibeni, A. Pazzaglia, M. Beghi, M. Passoni, *Nucl. Fusion* **2018**, *58*, 036019.
[43] N. W. Ashcroft, N. D. Mermin, S. Rodriguez, *Am. J. Phys.* **1978**, *46*, 116.
[44] a) J. Xu, P. Zou, D. Kang, W. Wang, A. Wang, *Opt. Laser Technol.* **2022**, *149*, 107906; b) J. D. Trejos, L. A. Reyes, C. Garza, P. Zambrano, O. Lopez-Botello, *Rapid Prototyping Journal* **2020**, *26*, 1555.
[45] L. Peng, M. Li, P. Wang, X. Li, Y. Zhang, M. He, C. Zhou, H. Zhang, S. Chen, *AIP Adv.* **2023**, *13*, 065018.

